

ArtPro: Self-Supervised Articulated Object Reconstruction with Adaptive Integration of Mobility Proposals

Xuelu Li^{1*} Zhaonan Wang^{1*} Xiaogang Wang^{2†} Lei Wu¹ Manyi Li^{1†} Changhe Tu¹

¹Shandong University ²Southwest University

{axtluli, d_wzn}@mail.sdu.edu.cn wangxiaogang@swu.edu.cn {i_lily, manyili, chtu}@sdu.edu.cn

Abstract

Reconstructing articulated objects into high-fidelity digital twins is crucial for applications such as robotic manipulation and interactive simulation. Recent self-supervised methods using differentiable rendering frameworks like 3D Gaussian Splatting remain highly sensitive to the initial part segmentation. Their reliance on heuristic clustering or pre-trained models often causes optimization to converge to local minima, especially for complex multi-part objects. To address these limitations, we propose ArtPro, a novel self-supervised framework that introduces adaptive integration of mobility proposals. Our approach begins with an over-segmentation initialization guided by geometry features and motion priors, generating part proposals with plausible motion hypotheses. During optimization, we dynamically merge these proposals by analyzing motion consistency among spatial neighbors, while a collision-aware motion pruning mechanism prevents erroneous kinematic estimation. Extensive experiments on both synthetic and real-world objects demonstrate that ArtPro achieves robust reconstruction of complex multi-part objects, significantly outperforming existing methods in accuracy and stability.

1. Introduction

Articulated objects such as cabinets, laptops, and scissors are ubiquitous in our daily lives. Creating their high-fidelity digital twins, including accurate reconstructions of part geometry, appearance, and kinematic structure, is the cornerstone for enabling robotic manipulation, virtual reality, and interactive scene simulation. However, this task remains highly challenging, as it requires jointly solving a set of intertwined sub-problems: part segmentation, motion parameter estimation, as well as high-quality appearance and geometry reconstruction.

Existing reconstruction approaches largely fall into two

*Equal contribution. †Corresponding author.

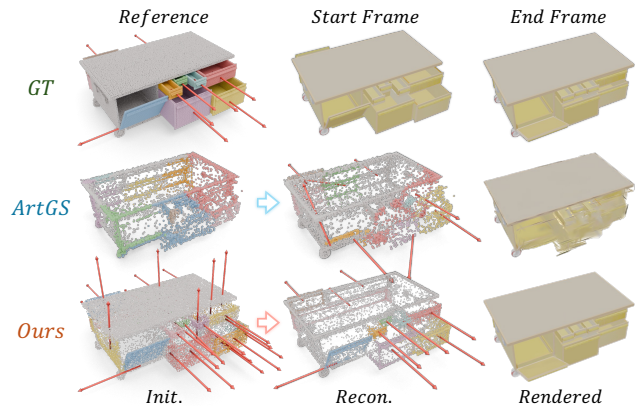


Figure 1. Existing methods like ArtGS [33] are highly sensitive to initial part segmentation, leading to inaccurate motion and geometry. Our method, ArtPro, leverages a prior-guided mobility initialization and adaptively merges mobility proposals during optimization, achieving robust reconstruction of complex multi-part articulated objects.

paradigms. On one hand, the feed-forward reconstruction methods [4, 5, 10, 19, 39, 41, 47] leverage powerful data-driven priors from diffusion or vision-language models to directly predict articulated structures from inputs like images or text, achieving remarkable inference speed. However, their generality is achieved either through coarse geometric abstractions or by being constrained to their training data. As a result, they often fail on unseen object categories or produce low-fidelity reconstructions, thus lacking instance-specific details. On the other hand, per-instance optimization methods [6, 32, 36, 46, 48], as represented by frameworks like NeRF or 3D Gaussian Splatting (3DGS), directly optimize the reconstruction for a specific instance without relying on those pre-trained models, achieving superior fidelity. Yet, they possess a critical weakness, i.e. **extreme sensitivity to the initialization of movable parts**. As shown in Figure 1, an initial segmentation from heuristic clustering that fails on complex multi-part objects can still yield a small rendering loss, causing the optimization

to converge to an incorrect kinematic structure (a local minimum). This strong dependency is particularly detrimental for objects with multiple movable parts, which severely hinders reconstruction efficiency and limits their practical utility in real-world applications.

To overcome these limitations, we introduce **ArtPro**, a robust and self-supervised framework for articulated object reconstruction based on 3DGS. Our core idea is to forgo the brittle “guess-the-segmentation-once” paradigm and instead adopt a more intelligent and robust “**propose-verify-merge**” pipeline. That is, we reframe part segmentation not as a fixed starting point, but as a dynamic process that is continuously refined during optimization.

The robustness and efficacy of ArtPro are driven by three key designs that form a self-correcting optimization system:

- **Prior-Guided Mobility Proposal Initialization:** We generate over-segmented mobility proposals by integrating geometry features with motion priors, establishing a robust initialization for subsequent optimization.
- **Adaptive Proposal Integration:** We dynamically merge mobility part proposals during the 3DGS optimization process by assessing motion consistency between adjacent regions, merging those that produce similar rendered results under exchanged motion parameters.
- **Collision-Aware Motion Pruning:** We introduce an active motion pruning mechanism that monitors inter-part collisions during optimization and calibrates problematic motion parameters to prevent local minima and ensure stable kinematic estimation.

Across extensive synthetic and real-world experiments, ArtPro demonstrates strong robustness and accuracy, consistently generating digital twins with precise geometry and kinematics. The method excels particularly on complex objects with multiple adjacent parts, significantly outperforming existing state-of-the-art alternatives.

2. Related Works

2.1. Understanding of 3D Articulated Objects

Prior research on articulated object understanding aims to infer part-level mobility and kinematic structures from sensory inputs, spanning several key directions. A substantial body of work focuses on *detecting movable parts*, either from single static images [17, 42] or by discovering articulation in videos [38]. Another major direction is *joint parameter estimation*, which recovers kinematic parameters such as joint axes, pivot point, and articulation angles. Further extending this line of work, methods have been developed for various inputs: some use point clouds [8, 18, 23, 28, 44, 50], others rely on RGB-D images from single or multiple views [1, 3, 13, 15, 16, 27], and some leverage videos [30] or 4D dynamic point clouds [31].

To overcome the limitations of passive perception, which

often suffer from ambiguous or insufficient viewpoints, active perception methods have been developed. These methods employ strategies that enable robots to actively interact with the environment or plan optimal viewing trajectories, thereby disambiguating the articulated structure and facilitating a more accurate estimation of its kinematic parameters [2, 51, 53, 54]. More recently, the field has increasingly leveraged the powerful reasoning capabilities of Vision-Language Models (VLMs) for articulated object understanding. By fine-tuning VLMs on these tasks, researchers have enabled them to directly estimate joint parameters and perform kinematic reasoning from a combination of visual and textual inputs [14, 39, 43]. However, despite producing shapes with plausible structures and joint parameters, these methods rely heavily on object datasets with extensive part-level annotations and consequently exhibit limited generalization ability.

2.2. Reconstruction of 3D Articulated Objects

Current methodologies for 3D articulated object reconstruction fall into two paradigms: *feed-forward* reconstruction and *per-instance optimization*, each presenting a unique set of trade-offs between efficiency, generality, and fidelity.

The first paradigm employs *feed-forward* models to directly predict articulated structures from inputs such as single/multiple images [4, 5, 10, 12, 19, 25, 35, 37, 47, 55], text prompts [39, 41], or articulation graphs [26]. Leveraging the powerful data-driven priors from diffusion models [9, 22, 34] or vision-language models [21, 39, 43], these methods achieve remarkable inference speed. However, this efficiency comes at a significant cost. To ensure generality, they often rely on the coarse geometric abstractions, such as bounding boxes, primitive shapes, or parts retrieved from limited databases, which fundamentally limit their ability to reconstruct fine-grained, instance-specific geometry and high-fidelity appearances. Therefore, their output quality is bounded by the scope of their training data and the simplicity of their output representations.

In contrast, the second paradigm employs *per-instance optimization*, bypassing pre-trained feedforward models to directly optimize a reconstruction for a specific object instance. The popular strategy is to rely on implicit representations, Neural Radiance Fields (NeRF) [6, 36, 48] and, more recently, 3D Gaussian Splatting [33, 46]. However, the scalability of these methods is severely limited by their strong dependency on the initial part segmentation. This is particularly problematic for complex multi-part objects, where an imperfect initialization often causes the optimization to converge to incorrect kinematic structures, making them largely ineffective in practice. To address these limitations, we introduce ArtPro, a novel framework designed to overcome the aforementioned challenges by adaptively initializing and integrating mobility proposals.

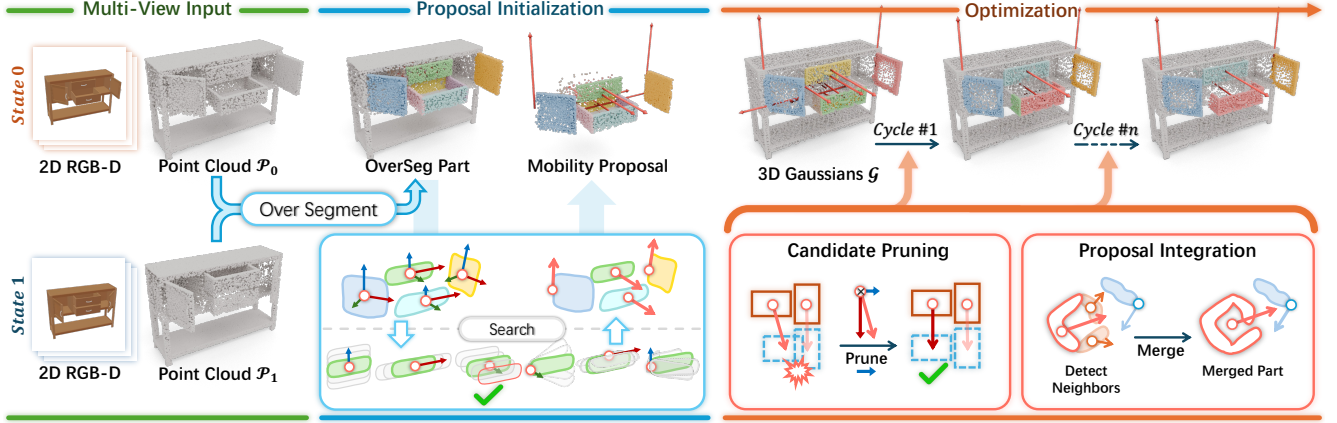


Figure 2. *ArtPro* reconstructs articulated objects from multi-view RGBD images of two states. The pipeline begins by initializing part-motion proposals through over-segmentation and a mixed-variable search. These proposals are then refined via a self-supervised optimization that updates the parts and their motion parameters using transformable 3D Gaussians. The optimization incorporates motion pruning and proposal integration operations to calibrate motions and merge proposals into coherent movable parts. Finally, a post-processing refinement stabilizes the appearance, geometry, and motion parameters of the reconstruction.

3. Method

3.1. Problem Formulation

Our goal is to reconstruct realistic digital twins of articulated objects from captured multi-view images. As shown in Figure 2, the input comprises two motion states of an articulated object, each state represented by a set of RGBD images. We parameterize the object states using a continuous variable t , and consider the two given states as the start ($t = 0$) and end ($t = 1$), respectively. Thus, any $t \in (0, 1)$ represents an intermediate state. Assuming the object contains one static part and M movable parts, the output of our approach consists of the segmented parts and their motion parameters, enabling realistic motion simulation of the reconstructed object.

The segmented parts are encoded using the 3D Gaussian Splatting (3DGS) representation. Specifically, in addition to the vanilla Gaussian parameters, we define part-aware probability fields and assign probability values for the Gaussian centered at x_i : $P_s(x_i)$ indicating its likelihood of belonging to the static part, and $\{P_m(x_i)\}_{m=1}^M$ for the movable parts. In this way, we assign the Gaussians to different parts based on the conditional probability

$$\hat{P}_m(x_i) = \frac{P_m(x_i)}{\sum_{k=1}^M P_k(x_i)}, \quad (1)$$

$$\mathcal{G}_m = \left\{ g_i \in \mathcal{G} \mid \hat{P}_m(x_i) > \epsilon \right\},$$

where \mathcal{G}_m denotes the m -th movable part, $\epsilon = 0.01$ is the threshold, x_i is the center of Gaussian $g_i \in \mathcal{G}$. The union of all the Gaussians \mathcal{G} represents the whole object.

The part motion parameters are defined according to the joint types. For prismatic joints, the motion of the movable

part is parameterized by a translation vector $t_m \in \mathcal{R}^3$. For revolute joints, the motion parameter is defined as a 6DoF rotation $r_m \in \mathcal{R}^6$ [56] and a center position $c_m \in \mathcal{R}^3$. Put them together, we can apply the rigid transformation of part m to a Gaussian g_i centered at x_i :

$$\hat{x}_i = R_m(x_i - c_m) + c_m + t_m, \quad \hat{q}_i = R_m \otimes q_i, \quad (2)$$

where R_m is the rotation matrix of r_m and q_i is the quaternion parameter of the Gaussian g_i .

With the above representation, we can apply the motion parameters to transform the articulated object \mathcal{G}

$$\hat{\mathcal{G}} = \mathcal{T}(\mathcal{G}). \quad (3)$$

To render the transformed articulated object $\hat{\mathcal{G}}$ with 3DGS differentiable rasterizer, we assign the adjusted opacity values $\hat{\alpha}_i = \hat{P}_m(x_i)\alpha_i$ and $\hat{\alpha}_i = P_s(x_i)\alpha_i$ to the Gaussians of movable parts and static part, respectively. This allows us to optimize the parts and their motion parameters of the articulated object based on the multi-view RGBD images.

3.2. Mobility Proposal Initialization

Since each part is attached with its own motion parameters, the part initialization significantly impacts subsequent optimization. To achieve robust reconstruction of complex multi-part objects, our strategy is to initialize with an over-segmentation of mobility proposals, which are then progressively merged during the optimization process.

The process begins with the over-segmentation of point clouds $\mathcal{P}^t = \{\mathcal{P}^0, \mathcal{P}^1\}$, which are constructed from input multi-view depth maps. The movable set $\hat{\mathcal{P}}_0$ is obtained by selecting points in \mathcal{P}^0 whose nearest-neighbor distance to \mathcal{P}^1 exceeds a threshold τ . Next, n seed points are selected

from $\hat{\mathcal{P}}_0$ via farthest point sampling. We then utilize point-wise features from a pre-trained segmentation model [29] to grow n over-segmented parts around these seeds. Finally, we merge parts with more than 80% overlap to produce M movable part proposals $\{\hat{\mathcal{P}}_m\}$. Note that the proposal count M does not necessarily equal to the ground-truth part number of the object.

We initialize the motion parameters for these proposals based on the heuristic that joint axes are typically perpendicular to part surfaces or aligned with their edges. For each part \mathcal{P}_m , we extract its oriented bounding box (OBB) and three principal component axes $\{\mathcal{X}_m, \mathcal{Y}_m, \mathcal{Z}_m\}$. We then select the most reliable axis to initialize the motion parameters by solving a mixed-variable optimization problem:

$$\arg \min_{\hat{a}, \phi, d} \text{CD} \left(R_m(\hat{a}, \phi) (\hat{\mathcal{P}}_m - c) + c + d \cdot \hat{a} \rightarrow \mathcal{P}^1 \right), \quad (4)$$

where we jointly solve for the discrete joint axis choice $\hat{a} \in \{\mathcal{X}_m, \mathcal{Y}_m, \mathcal{Z}_m\}$, the rotation angle ϕ , and the translation magnitude d . Here, $R_m(\hat{a}, \phi)$ denotes the rotation about axis \hat{a} by angle ϕ , and c is the center of the OBB face closest to \mathcal{P}^1 . The objective is to minimize the one-sided Chamfer distance $\text{CD}(\rightarrow)$ between the transformed movable parts and the target point cloud \mathcal{P}^1 . The variables are constrained to $d \in [-0.5, 0.5]$ meters and $\phi \in [-80^\circ, 80^\circ]$.

After obtaining the optimal solution, the motion parameters are initialized to an intermediate state as

$$R_m \leftarrow R_m(\hat{a}, \phi/2), \quad t_m \leftarrow (d/2) \cdot \hat{a}, \quad c_m \leftarrow c, \quad (5)$$

which helps stabilize the subsequent optimization by reducing the transformation magnitude to half.

3.3. Adaptive Proposal Integration Optimization

We propose an adaptive optimization algorithm to progressively merge initial mobility proposals, ultimately determining the coherent movable parts of the articulated object. As in Figure 2, the algorithm begins by establishing associations between the Gaussian primitives and the initialized proposals. It then refines these proposals through an adaptive optimization cycle, which consists of three key components: (1) *Gaussian primitive optimization*, which is the main body of the cycle, refines the segmentation and motion parameters of the proposals by iteratively updating the Gaussian primitives. (2) *Motion pruning operation* calibrates the motion parameters of the part proposals based on their motion trajectories. (3) *Proposal integration operation* merges pairs of proposals that belong to the same part and updates the associated Gaussian primitives. The cycle repeats until no proposals can be merged.

Gaussian-Proposal Association. We initialize two sets of Gaussian primitives from the point clouds \mathcal{P}^0 and \mathcal{P}^1 . Following [33], we assign the part-assignment probability for each Gaussian primitive using a Gaussian Mixture

Model (GMM). Specifically, the region of the m -th movable part proposal is represented by a Gaussian component $\mathcal{N}(\mu_m, \Sigma_m)$ with a positive mixture weight $\omega_m \in \mathbb{R}^+$. μ_m and Σ_m are initialized from the mean and variance of the point set $\hat{\mathcal{P}}_m$. The likelihood of a Gaussian primitive located at x belonging to movable part m is then given by

$$P_m(x) = \omega_m \cdot \mathcal{N}(x; \mu_m, \Sigma_m). \quad (6)$$

And that of the static part $P_s(x)$ is initialized as zero. This probabilistic association allows us to assign the Gaussians to the parts as described in Section 3.1 and transform Gaussian primitives according to the motion parameters.

Gaussian Primitive Optimization. The goal of this optimization is to iteratively refine the parameters of Gaussian primitives and their associated proposal motion parameters. In each iteration, we transform the Gaussians from the start state to the end state as described in Section 3.1 and render them with the differentiable rasterizer. Therefore, we obtain the Gaussian sets \mathcal{G} , their centers $\{x_i\}$, and the rendered images of the transformed articulated object.

We define a series of loss terms as the optimization objectives. The RGBD image loss \mathcal{L}_I and one-sided chamfer distance loss \mathcal{L}_{cd} encourage the transformed Gaussians to align with the underlying surface of the end state, in order to ensure the reconstruction fidelity and enable the following proposal integration by checking the spatial relation of Gaussian centers. The part contrastive loss \mathcal{L}_{pc} encourages the assignment of each Gaussian to a single dominant part by suppressing the probabilities of all non-maximum part proposals. The local smoothness loss \mathcal{L}_{ls} enforces spatial smoothness on the static part probability field by encouraging similar values for neighboring Gaussian primitives. The regularization term \mathcal{L}_{reg} encourages the compactness of each part by regularizing the part probabilities to align with a Gaussian distribution.

Finally, the objective function of the optimization is

$$\mathcal{L} = \mathcal{L}_I + \lambda_{cd} \mathcal{L}_{cd} + \lambda_{pc} \mathcal{L}_{pc} + \lambda_{ls} \mathcal{L}_{ls} + \lambda_{reg} \mathcal{L}_{reg}. \quad (7)$$

The detailed formulation of each loss term is presented in the supplementary material.

Motion Pruning Strategy. We calibrate the joint axes every 100 iterations during the Gaussian primitive optimization by measuring the overlap volume between the proposal pairs along their motion trajectories. It prevents the optimization from becoming stuck in local minima.

Specifically, for parts i and j , we compute their oriented bounding boxes (OBBs) in both the original (i.e. b_i^0, b_j^0) and transformed states (i.e. b_i^1, b_j^1). The overlap volumes between the two parts in these states are calculated as $v_{i,j}^0 = \text{Vol}(b_i^0 \cap b_j^0)$ and $v_{i,j}^1 = \text{Vol}(b_i^1 \cap b_j^1)$. A collision is flagged if the overlap volume of the end state is larger than that of the start state, i.e. $\Delta v_{i,j} = v_{i,j}^1 - v_{i,j}^0 > \tau_v$ with $\tau_v =$

10^{-4} . Once a collision is detected, the colliding axis a_{col} is identified as the principal axis of the OBB that exhibits the largest projection of the relative translation vector between the two parts. The motion parameters are then calibrated as follows to resolve the collision.

For a *prismatic joint*, the component of the translation vector t_m along the colliding axis a_{col} is pruned by projecting it onto the plane orthogonal to a_{col} :

$$t_m \leftarrow t_m - (t_m \cdot a_{\text{col}})a_{\text{col}}. \quad (8)$$

For a *revolute joint*, the proposals with near-identity rotation angles (e.g., less than 5°) are suppressed by resetting the rotation axis to align with the nearest OBB edge and halving the rotation angle to avoid the mutual influence between the two joint types.

In addition, we enforce a hard constraint on the joint type after 4K iterations. Thus, we set and fix t_m as zero for revolute joints and R_m as identity matrix for prismatic joints.

Proposal Integration Operation. We identify and merge proposal pairs that are both spatially adjacent and kinematically consistent. This is conducted every 5K iterations of the Gaussian primitive optimization.

The spatial adjacency between two proposals, \mathcal{G}_i and \mathcal{G}_j , is determined by performing the k -nearest neighbor search (with $k = 8$) over the union of all movable Gaussian centers $\cup\{\mathcal{G}_m\}$. Specifically, for each point x in \mathcal{G}_i , if any of its eight nearest neighbors belongs to a different movable part \mathcal{G}_j , then \mathcal{G}_i and \mathcal{G}_j are considered adjacent.

To evaluate motion consistency between an adjacent pair ($\mathcal{G}_i, \mathcal{G}_j$), we define a score function based on the L1 distance between rendered depth maps. The score $S(\mathcal{T})$ for a given motion parameters \mathcal{T} is formulated as the sum of L1 errors across all training views v of the end state:

$$S(\mathcal{T}) = \sum_{\mathcal{D}_v \in \{\mathcal{D}_i^1\}} |D_v(\mathcal{T}(\mathcal{G})) - \mathcal{D}_v|, \quad (9)$$

where $D_v(\mathcal{T}(\mathcal{G}))$ is the rendered depth map from viewpoint v , and \mathcal{D}_v is the corresponding ground-truth depth map at the end state ($t = 1$). For a pair ($\mathcal{G}_i, \mathcal{G}_j$), we compute two scores: the score with their current motion parameters, $S(\mathcal{T})$, and the score when the motion of part i is replaced by that of part j , denoted as $S(\mathcal{T}^{(j \rightarrow i)})$. The integration criterion is that their score variation falls below a predefined threshold τ , i.e., $|S(\mathcal{T}_i^{(i)}) - S(\mathcal{T}_i^{(j)})| < \tau_{\text{merge}} = 10^{-3}$. If a part \mathcal{G}_i has multiple adjacent parts eligible for merging, it is merged with the neighbor proposal \mathcal{G}_j for which the score variation is the smallest. This strategy ensures that we integrate only spatially adjacent parts with empirically consistent motions, effectively preventing spurious merges caused by minor rendering score jitter.

When integrating two part proposals, we merge \mathcal{G}_i and \mathcal{G}_j , and use the union of their Gaussian centers to initialize

the updated OBB and part probability field $P_{\text{new}}(x)$. The motion of the integrated part is updated as that of \mathcal{G}_j .

3.4. Post-Processing Refinement

After repeating the adaptive optimization cycle process several times to progressively integrate the proposals into movable parts, we conduct the Gaussian primitive optimization again as the post-processing refinement to obtain the accurate reconstruction. We follow the procedures of the Gaussian primitive optimization as described in Section 3.3 with a modified objective function.

The objective function includes the RGBD loss at both states $t = \{0, 1\}$. And we introduce a collision loss \mathcal{L}_{col} to avoid the collision between the movable and static parts of transformed object $\mathcal{T}(\mathcal{G})$. Thus the objective function is

$$\mathcal{L} = \mathcal{L}_I(\mathcal{G}) + \mathcal{L}_I(\mathcal{T}(\mathcal{G})) + \lambda_c \mathcal{L}_{\text{col}} \quad (10)$$

Detailed formulations are in the supplementary material.

4. Experiments

4.1. Settings

Datasets. We evaluate all the methods with articulated objects collected from the datasets of existing works [24, 33], including two-part objects and multi-part objects. In addition, we select 8 multi-part objects with 3-11 parts from the PartNet-Mobility dataset [49]. These articulated objects contain multiple parts with diverse motion structures and close locations, which poses particular challenges for reconstructing their accurate articulation structures.

Metrics. Following the evaluation protocol of ArtGS [33], we assess performance with the metrics of both mesh reconstruction and articulation estimation. For mesh reconstruction, we uniformly sample 10K points on the reconstructed mesh and the ground-truth mesh, then compute the chamfer distance for the whole object (CD-w), the static parts (CD-s), and the movable parts (CD-m). For articulation estimation, we compute the angular error (Axis Ang.) and distance (Axis Pos.) between the predicted and ground-truth joint axes, with the latter only for revolute joints. We also report part motion error (Part Motion), measuring rotational geodesic distance error (in degrees) for revolute joints and Euclidean distance error (in meters) for prismatic joints.

4.2. Comparisons

4.2.1. Comparison on Two-part Objects

The quantitative comparison with PARIS [24], ArticulatedGS [11], DTA [45], ArtGS [33], is presented in the supplementary material, showing that the 3DGS-based approaches produce competitive reconstruction results. Figure 3 provides the visual results of two-part objects using ArtGS [33] and our approach. It demonstrates that the

Table 1. Quantitative evaluation on our dataset. Lower(↓) is better on all metrics. We mark all joint type prediction errors and movable part count prediction errors with **F**. Window-103238 and Table-34610 are prismatic with no Axis Pos.

		Table 34178 (5 parts)	Storage 40417 (7 parts)	Window 103238 (3 parts)	Table 23372 (5 parts)	Storage 45759 (5 parts)	Table 33116 (4 parts)	Table 34610 (6 parts)	Storage 47585 (11 parts)	All
Axis Ang	DTA [45]	46.62	20.40	4.60	33.58	6.10	2.17	34.19	31.74	22.42
	ArtGS [33]	4.64	F	0.02	39.52	16.68	0.04	F	0.97	8.70 ^F
	Ours	0.05	0.07	0.06	0.06	0.03	0.02	0.09	0.16	0.07
Axis Pos	DTA [45]	21.68	3.37	-	2.90	0.66	0.01	-	1.15	4.96
	ArtGS [33]	1.42	F	-	1.46	0.05	0.00	-	0.00	0.32 ^F
	Ours	0.00	0.00	-	0.00	0.00	0.00	-	0.00	0.00
Part Motion	DTA [45]	25.65	30.17	0.26	12.79	32.92	0.11	0.10	2.51	13.07
	ArtGS [33]	11.42	F	0.20	15.21	13.01	0.01	F	27.65	9.50 ^F
	Ours	0.09	0.08	0.00	0.02	0.05	0.04	0.00	0.00	0.04
CD-s	DTA [45]	1.38	4.37	7.52	1.75	3.70	1.95	2.89	5.15	3.59
	ArtGS [33]	1.87	0.90	6.61	2.81	1.83	1.60	2.55	2.97	2.64
	Ours	0.42	0.36	0.11	0.47	0.37	0.65	1.15	3.21	0.84
CD-m	DTA [45]	F	F	65.60	F	F	0.85	48.06	F	38.17 ^F
	ArtGS [33]	16.91	1,316.00	330.98	541.48	29.37	1.33	253.04	273.40	345.31
	Ours	3.58	0.26	0.14	2.20	0.48	0.15	13.01	11.11	3.86
CD-w	DTA [45]	1.06	0.84	0.44	0.96	0.85	1.47	0.91	2.36	1.11
	ArtGS [33]	2.05	1.00	0.64	2.69	1.67	1.97	2.02	4.08	2.02
	Ours	0.45	0.33	0.12	0.41	0.36	0.30	1.16	2.13	0.65

Table 2. ArtGS-Multi dataset [33] results. Lower(↓) is better on all metrics. Table-25493 is prismatic with no Axis Pos.

		Table 25493 (4 parts)	Table 31249 (5 parts)	Storage 45503 (4 parts)	Storage 47468 (7 parts)	Oven 101908 (4 parts)	All
Axis Ang	DTA	24.35	20.62	51.18	19.07	17.83	26.61
	ArtGS	1.16	0.04	0.02	0.14	0.04	0.28
	Ours	0.08	0.04	0.03	0.07	0.01	0.05
Axis Pos	DTA	-	4.20	2.44	0.31	6.51	3.37
	ArtGS	-	0.00	0.00	0.02	0.01	0.01
	Ours	-	0.00	0.00	0.00	0.01	0.00
Part Motion	DTA	0.12	30.80	43.77	10.67	31.80	23.43
	ArtGS	0.00	0.01	0.03	0.62	0.23	0.18
	Ours	0.00	0.02	0.03	0.09	0.09	0.05
CD-s	DTA	0.59	1.39	5.74	0.82	1.17	1.94
	ArtGS	0.74	1.22	0.75	0.67	1.08	0.89
	Ours	0.20	0.32	0.24	0.18	0.55	0.30
CD-m	DTA	104.38	230.38	246.63	476.91	359.16	283.49
	ArtGS	3.53	3.09	0.13	3.70	0.25	2.14
	Ours	0.14	1.88	0.08	2.26	0.11	0.89
CD-w	DTA	0.55	1.00	0.88	0.71	1.01	0.83
	ArtGS	0.74	1.16	0.88	0.70	1.03	0.90
	Ours	0.18	0.39	0.25	0.17	0.47	0.29

optimization results of ArtGS (and other 3DGS-based approaches) relies heavily on the initialization. By contrast, our method adaptively merge the over-segmented part proposals during optimization, thus achieving more robust reconstruction results.

It is worth noting that our method doesn't necessarily merge the disconnected components together, such as the Blade-103706 shown in second row of Figure 3. For this case, although the slider and blade are assigned as different parts, our method still successfully estimates their accurate motion parameters due to the adaptive proposal integration.

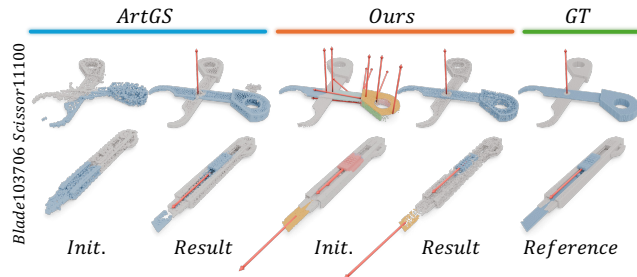


Figure 3. The part initialization and reconstruction results of ArtGS [33] and ours on two-part objects. Although our approach doesn't merge the two disadjacent movable parts (second row), we still obtain accurate motion and geometry reconstruction.

4.2.2. Comparison on Multi-part Objects

We further evaluate the performance of multi-part object reconstruction methods, i.e. DTA [45] and ArtGS [33]. Table 2 and Table 1 reports the quantitative results. Since DTA suffers from movable part identification and axis prediction as the number of parts increases, it leads to significant deviations in the motion axes. This in turn results in greater errors for part motion estimation and movable part reconstruction. The other two methods, ArtGS and ours, both achieve accurate reconstruction and motion estimation in many cases. However, for complex objects with adjacent movable parts, as reported in Table 1, ArtGS leads to incorrect motion estimations and thus larger reconstruction errors, while our method constantly achieves robust estimation for all the movable parts.

Figure 4 shows the reconstructed objects at different

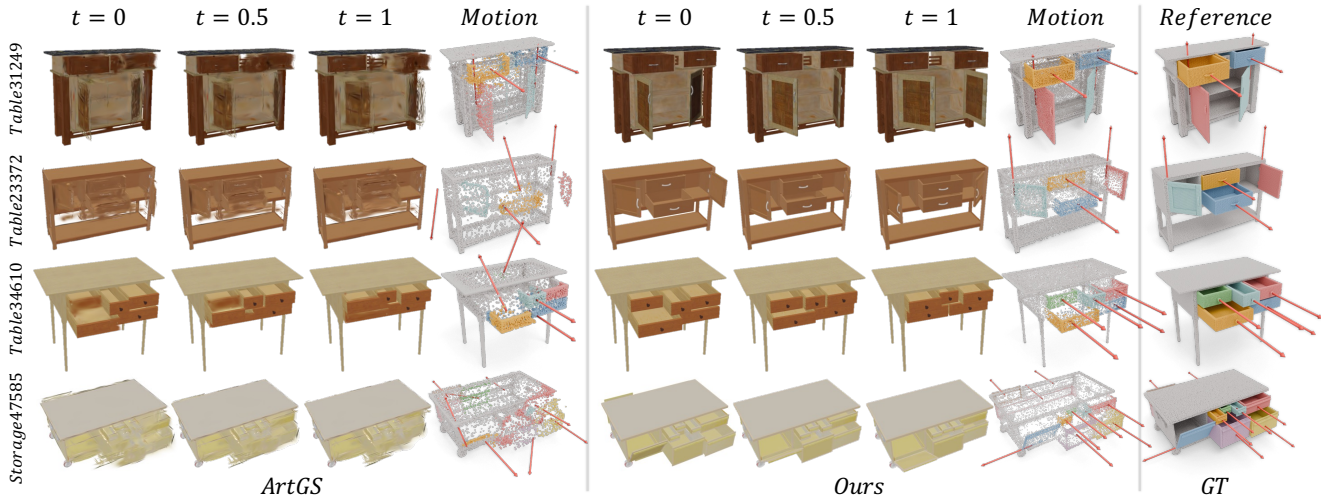


Figure 4. The reconstructed articulated objects in different motion states ($t = \{0, 0.5, 1\}$) and their part-motion structures.

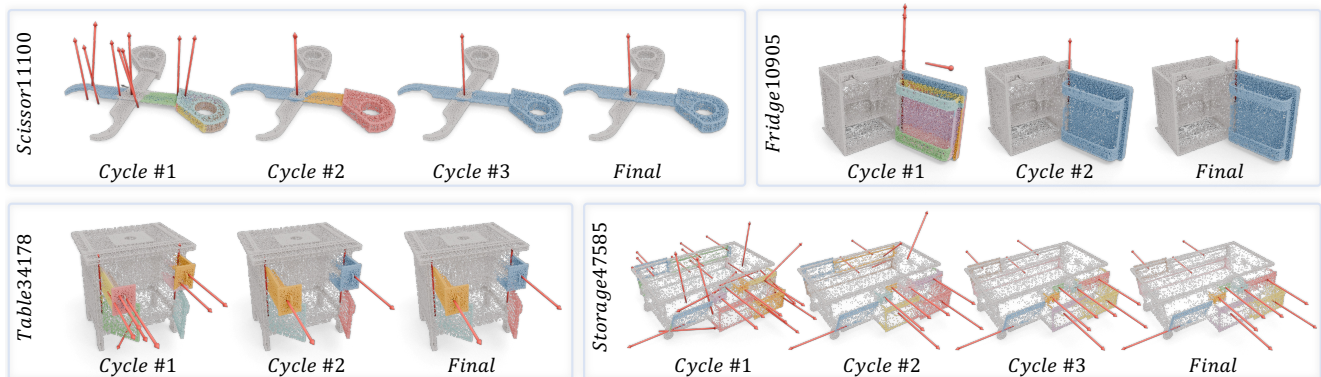


Figure 5. The intermediate results during our adaptive proposal integration optimization. We show the optimized Gaussians (with their center points) and the estimated motions before the proposal integration operation at each cycle.

states and their motion structures. Comparing these multi-part articulated objects, ArtGS often fails and falls trapped in a local optimum early during optimization, since the clustering-based algorithm cannot provide a stable initialization. By contrast, our over-segmentation-based initialization can segment potential part proposals from the object, and effectively merge them into complete parts during the adaptive integration optimization. Thus, our method produces robust reconstructions for all the multi-part objects.

In Figure 5, we show the intermediate results of movable parts being adaptively integrated under over-segmentation initialization. For complex inputs, our method can merge similar parts based on motion parameters optimized after some iteration steps, resulting in complete movable parts with only a few cycles.

4.2.3. Results on Real-World Objects

We additionally evaluate our approach on real-world articulated objects. Specifically, we collected 200 RGB images, 100 for each state, around the target object and utilized the

pre-trained depth-anything-V2 model [52] to estimate the calibrated depth. Then, we use SAM2 [40] to obtain the object masks. Finally, we take the processed multi-view RGBD images of two states as the input of our approach.

Figure 7 presents the reconstruction results of the real-world multi-part objects. Our method achieves robust and accurate results for them. More importantly, the superior mobility reconstruction ensures the correct articulated object with high-quality parts and motion parameters.

4.3. Ablation Studies

As listed in Table 3, we conduct the following ablation experiments to validate the effectiveness of our key designs:

- The baseline (#1) applies DBSCAN clustering [7] (with the ground-truth part number M) to separate the movable parts and assign identity transformation as initialization, then optimize the Gaussians and motion parameters with the same setting of our approach, but without the adaptive proposal integration and motion pruning strategy. As shown in Figure 6, once the movable parts are incorrectly

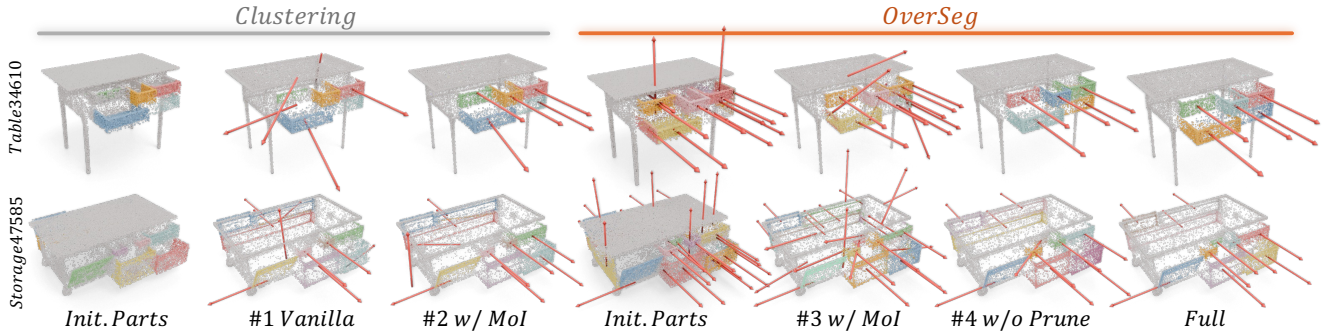


Figure 6. Ablation study results. To compare with our *OverSeg* initialization, we use DBSCAN [7] as our clustering implementation, denoted *Vanilla*. We further add motion initialization to *Vanilla* and *OverSeg* baseline, denoted *w/ MoI*. Finally, we removed the pruning strategy from *Full* (*w/o Prune*) to verify its significant.

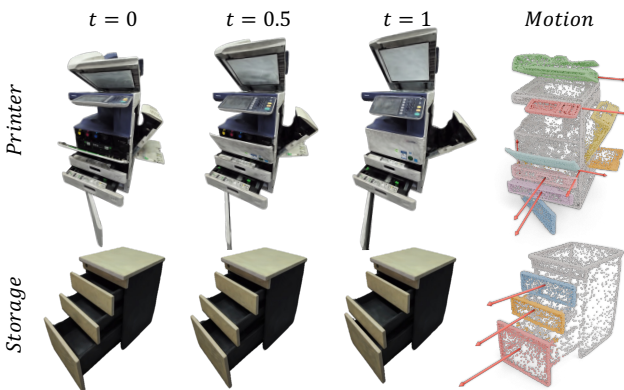


Figure 7. Reconstructed results of real-world articulated objects.

segmented or located close to each other, it sometimes causes missing parts or converges to local minima, leading to failed motion estimation and inaccurate geometry.

- We then add our proposal initialization algorithm (*MoI*) into the baseline setting. Baseline (#2) refers to initializing our proposals with the given part number M , while baseline (#3) leverages our over-segmentation initialization without knowing the ground-truth part number. In Figure 6, the third col validates that our method leads to more reasonable mobility initialization and thus more accurate final reconstructions, while the fourth col exposes the remaining problem with unstable part initialization.
- We further insert our adaptive proposal integration strategy (*Merge*) in baseline (#4). It achieves robustness to the proposals of various complex articulated objects. However, some of the objects still exhibit relatively larger reconstruction errors, due to unstable motion initialization and the lack of collision-aware constraints to calibrate the parameters of adjacent parts, such as the middle three drawers of *Storage* (*w/o Prune*) in Figure 6.
- By contrast, our full approach effectively prevents incorrect motion estimation caused by collisions between adjacent parts. By maximally leveraging motion priors

Table 3. Quantitative evaluation of the ablation study. Lower(↓) is better on all metrics. To evaluate the results with arbitrary numbers of movable parts, we compute CD between the merged movable results and GT movable parts, denoted as $\overline{CD-m}$.

Case	OverSeg	MoI	Merge	Prune	CD-s	$\overline{CD-m}$	CD-w
#1					1.46	9.27	0.93
#2		✓			1.04	6.97	0.67
#3	✓	✓			0.87	5.01	0.71
#4	✓	✓	✓		0.85	4.57	0.67
Full	✓	✓	✓	✓	0.84	3.63	0.65

of man-made objects, our method achieves robust reconstruction performance for all the multi-part objects.

5. Conclusion

We introduced ArtPro, a self-supervised framework based on 3D Gaussian Splatting for robustly reconstructing high-fidelity digital twins of articulated objects. Our method begins with an over-segmented set of part proposals and adaptively merges them during optimization through motion-consistency analysis and collision-aware pruning. This strategy significantly improves motion estimation and reconstruction quality, especially for complex objects with multiple parts and diverse articulations, as validated through extensive experiments on synthetic and real-world datasets.

However, our approach currently relies primarily on motion cues between two object states, which may be insufficient for disambiguating parts with perfectly symmetric or very subtle motions. Additionally, the reconstruction quality, particularly at part boundaries, remains sensitive to the accuracy of input sensor data. Future work will explore the integration of stronger semantic priors, geometry constraints, and multi-state tracking to address these challenges and further expand the applicability of our method.

References

- [1] Ben Abbatematteo, Stefanie Tellex, and George Konidaris. Learning to generalize kinematic models to novel objects. In *Proceedings of the 3rd Conference on Robot Learning*, 2019. 2
- [2] Ankan Kumar Bhunia, Changjian Li, and Hakan Bilen. Interactive anomaly detection for articulated objects via motion anticipation. In *The Thirty-ninth Annual Conference on Neural Information Processing Systems*. 2
- [3] Yuchen Che, Ryo Furukawa, and Asako Kanezaki. Op-align: Object-level and part-level alignment for self-supervised category-level articulated object pose estimation. In *European Conference on Computer Vision*, pages 72–88. Springer, 2024. 2
- [4] Zoey Chen, Aaron Walsman, Marius Memmel, Kaichun Mo, Alex Fang, Karthikeya Vemuri, Alan Wu, Dieter Fox, and Abhishek Gupta. Urdformer: A pipeline for constructing articulated simulation environments from real-world images. *arXiv preprint arXiv:2405.11656*, 2024. 1, 2
- [5] Tianyuan Dai, Josiah Wong, Yunfan Jiang, Chen Wang, Cem Gokmen, Ruohan Zhang, Jiajun Wu, and Li Fei-Fei. Automated creation of digital cousins for robust policy learning. *arXiv preprint arXiv:2410.07408*, 2024. 1, 2
- [6] Jianning Deng, Kartic Subr, and Hakan Bilen. Articulate your nerf: Unsupervised articulated object modeling via conditional view synthesis. *Advances in Neural Information Processing Systems*, 37:119717–119741, 2024. 1, 2
- [7] Martin Ester, Hans-Peter Kriegel, Jörg Sander, Xiaowei Xu, et al. A density-based algorithm for discovering clusters in large spatial databases with noise. In *kdd*, pages 226–231, 1996. 7, 8
- [8] Lian Fu, Ryoichi Ishikawa, Yoshihiro Sato, and Takeshi Oishi. Capt: Category-level articulation estimation from a single point cloud using transformer, 2024. 2
- [9] Daoyi Gao, Yawar Siddiqui, Lei Li, and Angela Dai. Meshart: Generating articulated meshes with structure-guided transformers. In *Proceedings of the Computer Vision and Pattern Recognition Conference*, pages 618–627, 2025. 2
- [10] Mingju Gao, Yike Pan, Huan-ang Gao, Zongzheng Zhang, Wenyi Li, Hao Dong, Hao Tang, Li Yi, and Hao Zhao. Partm: Modeling part-level dynamics with large cross-state reconstruction model. In *Proceedings of the Computer Vision and Pattern Recognition Conference*, pages 7004–7014, 2025. 1, 2
- [11] Junfu Guo, Yu Xin, Gaoyi Liu, Kai Xu, Ligang Liu, and Ruizhen Hu. Articulatedgts: Self-supervised digital twin modeling of articulated objects using 3d gaussian splatting. In *Proceedings of the Computer Vision and Pattern Recognition Conference*, pages 27144–27153, 2025. 5, 1, 2
- [12] Nick Heppert, Muhammad Zubair Irshad, Sergey Zakharov, Katherine Liu, Rares Andrei Ambrus, Jeannette Bohg, Abhinav Valada, and Thomas Kollar. Carto: Category and joint agnostic reconstruction of articulated objects. In *Proceedings of the IEEE/CVF Conference on Computer Vision and Pattern Recognition*, pages 21201–21210, 2023. 2
- [13] Ruizhen Hu, Wenchao Li, Oliver Van Kaick, Ariel Shamir, Hao Zhang, and Hui Huang. Learning to predict part mobility from a single static snapshot. *ACM Transactions On Graphics (TOG)*, 36(6):1–13, 2017. 2
- [14] Siyuan Huang, Haonan Chang, Yuhan Liu, Yimeng Zhu, Hao Dong, Peng Gao, Abdeslam Boularias, and Hongsheng Li. A3vlm: Actionable articulation-aware vision language model. *arXiv preprint arXiv:2406.07549*, 2024. 2
- [15] Ajinkya Jain, Rudolf Lioutikov, Caleb Chuck, and Scott Niekum. Screwnet: Category-independent articulation model estimation from depth images using screw theory. In *2021 IEEE International Conference on Robotics and Automation (ICRA)*, pages 13670–13677. IEEE, 2021. 2
- [16] Ajinkya Jain, Stephen Giguere, Rudolf Lioutikov, and Scott Niekum. Distributional depth-based estimation of object articulation models. In *Conference on Robot Learning*, pages 1611–1621. PMLR, 2022. 2
- [17] Hanxiao Jiang, Yongsun Mao, Manolis Savva, and Angel X Chang. Opd: Single-view 3d openable part detection. In *Computer Vision—ECCV 2022: 17th European Conference, Tel Aviv, Israel, October 23–27, 2022, Proceedings, Part XXXIX*, pages 410–426. Springer, 2022. 2
- [18] Zhenyu Jiang, Cheng-Chun Hsu, and Yuke Zhu. Ditto: Building digital twins of articulated objects from interaction. In *Conference on Computer Vision and Pattern Recognition (CVPR)*, 2022. 2
- [19] Yuki Kawana and Tatsuya Harada. Detection based part-level articulated object reconstruction from single rgbd image. *Advances in Neural Information Processing Systems*, 36:18444–18473, 2023. 1, 2
- [20] Bernhard Kerbl, Georgios Kopanas, Thomas Leimkuehler, and George Drettakis. 3d gaussian splatting for real-time radiance field rendering. *ACM Transactions on Graphics (TOG)*, 42:1–14, 2023. 1
- [21] Long Le, Jason Xie, William Liang, Hung-Ju Wang, Yue Yang, Yecheng Jason Ma, Kyle Vedder, Arjun Krishna, Dinesh Jayaraman, and Eric Eaton. Articulate-anything: Automatic modeling of articulated objects via a vision-language foundation model. *arXiv preprint arXiv:2410.13882*, 2024. 2
- [22] Jiahui Lei, Congyue Deng, Bokui Shen, Leonidas Guibas, and Kostas Daniilidis. Nap: Neural 3d articulation prior. *arXiv preprint arXiv:2305.16315*, 2023. 2
- [23] Xiaolong Li, He Wang, Li Yi, Leonidas J. Guibas, A. Lynn Abbott, and Shuran Song. Category-level articulated object pose estimation. In *Proceedings of the IEEE/CVF Conference on Computer Vision and Pattern Recognition*, pages 3706–3715, 2020. 2
- [24] Jiayi Liu, Ali Mahdavi-Amiri, and Manolis Savva. Paris: Part-level reconstruction and motion analysis for articulated objects. In *Proceedings of the IEEE/CVF International Conference on Computer Vision*, pages 352–363, 2023. 5, 1, 2
- [25] Jiayi Liu, Denys Iliash, Angel X Chang, Manolis Savva, and Ali Mahdavi-Amiri. Singapo: Single image controlled generation of articulated parts in objects. *arXiv preprint arXiv:2410.16499*, 2024. 2
- [26] Jiayi Liu, Hou In Ivan Tam, Ali Mahdavi-Amiri, and Manolis Savva. Cage: Controllable articulation generation. In *Proceedings of the IEEE/CVF Conference on Computer Vision and Pattern Recognition*, pages 17880–17889, 2024. 2

- [27] Liu Liu, Han Xue, Wenqiang Xu, Haoyuan Fu, and Cewu Lu. Toward real-world category-level articulation pose estimation. *IEEE Transactions on Image Processing*, 31:1072–1083, 2022. 2
- [28] Liu Liu, Jianming Du, Hao Wu, and Xun Yang. Category-level articulated object 9d pose estimation via reinforcement learning. *Proceedings of the 31st ACM International Conference on Multimedia*, pages 728–736, 2023. 2
- [29] Minghua Liu, Mikaela Angelina Uy, Donglai Xiang, Hao Su, Sanja Fidler, Nicholas Sharp, and Jun Gao. Partfield: Learning 3d feature fields for part segmentation and beyond. In *Proceedings of the IEEE/CVF International Conference on Computer Vision*, pages 9704–9715, 2025. 4
- [30] Qihao Liu, Weichao Qiu, Weiyao Wang, Gregory D Hager, and Alan L Yuille. Nothing but geometric constraints: A model-free method for articulated object pose estimation. *arXiv preprint arXiv:2012.00088*, 2020. 2
- [31] Shaowei Liu, Saurabh Gupta, and Shenlong Wang. Building rearticulable models for arbitrary 3d objects from 4d point clouds. In *Proceedings of the IEEE/CVF Conference on Computer Vision and Pattern Recognition*, pages 21138–21147, 2023. 2
- [32] Yu Liu, Baoxiong Jia, Ruijie Lu, Chuyue Gan, Huayu Chen, Junfeng Ni, Song-Chun Zhu, and Siyuan Huang. Videoartgs: Building digital twins of articulated objects from monocular video. *arXiv preprint arXiv:2509.17647*, 2025. 1
- [33] Yu Liu, Baoxiong Jia, Ruijie Lu, Junfeng Ni, Song-Chun Zhu, and Siyuan Huang. Artgs: Building interactable replicas of complex articulated objects via gaussian splatting. *arXiv preprint arXiv:2502.19459*, 2025. 1, 2, 4, 5, 6
- [34] Rundong Luo, Haoran Geng, Congyue Deng, Puhao Li, Zan Wang, Baoxiong Jia, Leonidas Guibas, and Siyuan Huang. Physpart: Physically plausible part completion for interactable objects. In *2025 IEEE International Conference on Robotics and Automation (ICRA)*, pages 12386–12393. IEEE, 2025. 2
- [35] Zhao Mandi, Yijia Weng, Dominik Bauer, and Shuran Song. Real2code: Reconstruct articulated objects via code generation. *arXiv preprint arXiv:2406.08474*, 2024. 2
- [36] Jiteng Mu, Weichao Qiu, Adam Kortylewski, Alan Yuille, Nuno Vasconcelos, and Xiaolong Wang. A-sdf: Learning disentangled signed distance functions for articulated shape representation. In *Proceedings of the IEEE/CVF International Conference on Computer Vision*, pages 13001–13011, 2021. 1, 2
- [37] Akshay Gadi Patil, Yiming Qian, Shan Yang, Brian Jackson, Eric Bennett, and Hao Zhang. Rosi: Recovering 3d shape interiors from few articulation images. *arXiv preprint arXiv:2304.06342*, 2023. 2
- [38] Shengyi Qian, Linyi Jin, Chris Rockwell, Siyi Chen, and David F. Fouhey. Understanding 3d object articulation in internet videos. In *Proceedings of the IEEE/CVF Conference on Computer Vision and Pattern Recognition*, pages 1599–1609, 2022. 2
- [39] Xiaowen Qiu, Jincheng Yang, Yian Wang, Zhehuan Chen, Yufei Wang, Tsun-Hsuan Wang, Zhou Xian, and Chuang Gan. Articulate anymesh: Open-vocabulary 3d articulated objects modeling. *arXiv preprint arXiv:2502.02590*, 2025. 1, 2
- [40] Nikhila Ravi, Valentin Gabeur, Yuan-Ting Hu, Ronghang Hu, Chaitanya Ryali, Tengyu Ma, Haitham Khedr, Roman Rädle, Chloe Rolland, Laura Gustafson, Eric Mintun, Junting Pan, Kalyan Vasudev Alwala, Nicolas Carion, Chao-Yuan Wu, Ross Girshick, Piotr Dollár, and Christoph Feichtenhofer. Sam 2: Segment anything in images and videos. *arXiv preprint arXiv:2408.00714*, 2024. 7
- [41] Jiayi Su, Youhe Feng, Zheng Li, Jinhua Song, Yangfan He, Botao Ren, and Botian Xu. Artformer: Controllable generation of diverse 3d articulated objects. In *Proceedings of the Computer Vision and Pattern Recognition Conference*, pages 1894–1904, 2025. 1, 2
- [42] Xiaohao Sun, Hanxiao Jiang, Manolis Savva, and Angel Xuan Chang. Opdmulti: Openable part detection for multiple objects. *arXiv preprint arXiv:2303.14087*, 2023. 2
- [43] Aditya Vora, Sauradip Nag, and Hao Zhang. Articulate that object part (atop): 3d part articulation via text and motion personalization. *arXiv preprint arXiv:2502.07278*, 2025. 2
- [44] Xiaogang Wang, Bin Zhou, Yahao Shi, Xiaowu Chen, Qingping Zhao, and Kai Xu. Shape2motion: Joint analysis of motion parts and attributes from 3d shapes. In *Proceedings of the IEEE/CVF Conference on Computer Vision and Pattern Recognition*, pages 8876–8884, 2019. 2
- [45] Yijia Weng, Bowen Wen, Jonathan Tremblay, Valts Blukis, Dieter Fox, Leonidas Guibas, and Stan Birchfield. Neural implicit representation for building digital twins of neuronal articulated objects. In *Proceedings of the IEEE/CVF Conference on Computer Vision and Pattern Recognition*, pages 3141–3150, 2024. 5, 6, 1, 2
- [46] Di Wu, Liu Liu, Zhou Linli, Anran Huang, Liangtu Song, Qiaojun Yu, Qi Wu, and Cewu Lu. Reartgs: Reconstructing and generating articulated objects via 3d gaussian splatting with geometric and motion constraints. *arXiv preprint arXiv:2503.06677*, 2025. 1, 2
- [47] Ruiqi Wu, Xinjie Wang, Liu Liu, Chunle Guo, Jiaxiong Qiu, Chongyi Li, Lichao Huang, Zhizhong Su, and Ming-Ming Cheng. Dipo: Dual-state images controlled articulated object generation powered by diverse data. *arXiv preprint arXiv:2505.20460*, 2025. 1, 2
- [48] Tianhao Wu, Fangcheng Zhong, Andrea Tagliasacchi, Forrester Cole, and Cengiz Oztireli. D²nerf: Self-supervised decoupling of dynamic and static objects from a monocular video. *Advances in neural information processing systems*, 35:32653–32666, 2022. 1, 2
- [49] Fanbo Xiang, Yuzhe Qin, Kaichun Mo, Yikuan Xia, Hao Zhu, Fangchen Liu, Minghua Liu, Hanxiao Jiang, Yifu Yuan, He Wang, et al. Sapien: A simulated part-based interactive environment. In *Proceedings of the IEEE/CVF conference on computer vision and pattern recognition*, pages 11097–11107, 2020. 5
- [50] Zihao Yan, Ruizhen Hu, Xingguang Yan, Luanmin Chen, Oliver Van Kaick, Hao Zhang, and Hui Huang. Rpm-net: recurrent prediction of motion and parts from point cloud. *arXiv preprint arXiv:2006.14865*, 2020. 2

- [51] Zihao Yan, Fubao Su, Mingyang Wang, Ruizhen Hu, Hao Zhang, and Hui Huang. Interaction-driven active 3d reconstruction with object interiors. *ACM Transactions on Graphics (TOG)*, 42(6):1–12, 2023. [2](#)
- [52] Lihe Yang, Bingyi Kang, Zilong Huang, Zhen Zhao, Xiaogang Xu, Jiashi Feng, and Hengshuang Zhao. Depth anything v2. *Advances in Neural Information Processing Systems*, 37:21875–21911, 2024. [7](#), [3](#)
- [53] Hongliang Zeng, Ping Zhang, Chengjiong Wu, Jiahua Wang, Tingyu Ye, and Fang Li. Mars: Multimodal active robotic sensing for articulated characterization. *arXiv preprint arXiv:2407.01191*, 2024. [2](#)
- [54] Can Zhang and Gim Hee Lee. Iaao: Interactive affordance learning for articulated objects in 3d environments. In *Proceedings of the Computer Vision and Pattern Recognition Conference*, pages 12132–12142, 2025. [2](#)
- [55] Ge Zhang, Or Litany, Srinath Sridhar, and Leonidas Guibas. Strobenet: Category-level multiview reconstruction of articulated objects. *arXiv preprint arXiv:2105.08016*, 2021. [2](#)
- [56] Yi Zhou, Connelly Barnes, Jingwan Lu, Jimei Yang, and Hao Li. On the continuity of rotation representations in neural networks. In *Proceedings of the IEEE/CVF conference on computer vision and pattern recognition*, pages 5745–5753, 2019. [3](#)

ArtPro: Self-Supervised Articulated Object Reconstruction with Adaptive Integration of Mobility Proposals

Supplementary Material

In this supplementary material, we first present the loss term formulations of Gaussian primitive optimization in Section A. Then, we present more two-part comparisons in Section B. In Section C and Section D, we provide more multi-part visualization and full initialization of our method on multi-part dataset. Finally, in Section E, we report the failure cases of our method.

A. Loss Terms of Gaussian Optimization

Below we present the detailed formulation of the loss terms used in the Gaussian primitive optimization, which are mentioned in Section 3.3 and 3.4 in the main paper.

The RGBD loss \mathcal{L}_I and the one-sided Chamfer Distance loss \mathcal{L}_{cd} encourage the transformed Gaussians to align with the underlying surface of the end state. We have

$$\begin{aligned} \mathcal{L}_D &= \log(1 + \|D_v(\mathcal{T}(\mathcal{G})) - \mathcal{D}_v\|_1) \\ \mathcal{L}_I &= \mathcal{L}_{3dgs}(\mathcal{T}(\mathcal{G})) + \mathcal{L}_D(\mathcal{T}(\mathcal{G})), \\ \mathcal{L}_{cd} &= \text{CD}(\cup\{x_m\} \rightarrow \mathcal{P}^1) \end{aligned} \quad (11)$$

where $D_v(\cdot)$ denotes the rendered depth map of view v , \mathcal{L}_{3dgs} is the RGB loss used in 3DGS [20], \mathcal{G} is the Gaussian sets, $\{x_m\}$ is the Gaussian centers of all movable $\{\mathcal{G}_m\}$, and \mathcal{P}^1 is the point cloud of state $t = 1$. We compute the loss \mathcal{L}_I between the rendered images of transformed Gaussian $\mathcal{T}(\mathcal{G})$ and GT RGBD to optimize the appearance, and use \mathcal{L}_{cd} to further improve the geometric quality.

The part contrastive loss \mathcal{L}_{pc} ensures each Gaussian be dominated by one distinctive part

$$\mathcal{L}_{pc} = \mathbb{E}_{\{x_i \in \mathcal{G}_m\}^M} \left[\frac{1}{M-1} \sum_{\substack{k=1 \\ k \neq m}}^M P_k(x_i) \right], \quad (12)$$

where, \mathcal{G}_m denotes the m -th movable part of $\{\mathcal{G}_m\}_{m=1}^M$, $P_k(x_i)$ is the probability that the point x_i belongs to the k -th movable part.

The local smoothness loss \mathcal{L}_{ls} aims to maintain consistent static part probability for the spatial neighbors $x_i, x_j \in \mathcal{G}$. It is formulated as

$$\mathcal{L}_{ls} = \mathbb{E}_{x_i \in \mathcal{G}, x_j \in \text{kNN}(x_i, \mathcal{G})} |P_s(x_i) - P_s(x_j)|, \quad (13)$$

where kNN denote k-nearest neighbors with $k = 20$. To avoid fragmented parts, we smooth the static probability field on the kNN-based neighborhood graph to obtain a locally consistent segmentation field.

The regularization term aims to encourage the compactness of the parts. It uses the mean $\{\hat{\mu}_m\}$ and variance scaling $\{\hat{s}_m\}$ of initialization $\{\hat{\mathcal{P}}_m\}$ to maintain the existence of p_m

$$\mathcal{L}_{reg} = \frac{1}{M} \sum_{m=1}^M \left[\lambda_\mu |\mu_m - \hat{\mu}_m| + \lambda_s \|s_m - \hat{s}_m\|_1 \right] \quad (14)$$

where, s_m is the scaling of variance Σ_m , and $\lambda_\mu = 0.5, \lambda_s = 0.1$ is loss weight.

In summary, the objective function of Gaussian primitive optimization in the adaptive proposal integration stage is:

$$\mathcal{L} = \mathcal{L}_I + \lambda_{cd} \mathcal{L}_{cd} + \lambda_{pc} \mathcal{L}_{pc} + \lambda_{ls} \mathcal{L}_{ls} + \lambda_{reg} \mathcal{L}_{reg}. \quad (15)$$

We use $\lambda_{CD} = 0.5, \lambda_{pc} = 0.1, \lambda_{ls} = 0.02$ and $\lambda_{reg} = 1.0$ in all the experiments presented in this paper.

We further define a collision loss \mathcal{L}_{col} , which avoids the collisions between the movable and static parts of the transformed object. It is formulated as

$$\begin{aligned} L_{col}(\mathcal{G}_i, \mathcal{G}_j) &= \mathbb{E}_{x \in \mathcal{G}_i, y \in \text{kNN}(x, \mathcal{G}_j)} |\hat{\alpha}_y|, \\ \mathcal{L}_{col} &= L_{col}(\mathcal{T}(\mathcal{G}_m), \mathcal{G}_s) + L_{col}(\mathcal{G}_s, \mathcal{T}(\mathcal{G}_m)), \end{aligned} \quad (16)$$

where $\mathcal{T}(\mathcal{G}_m)$ is the union of all movable parts of $\mathcal{T}(\mathcal{G})$, \mathcal{G}_s is the static part of $\mathcal{T}(\mathcal{G})$, α_y is the Gaussian opacity corresponding to center position y , and kNN is the set of k nearest neighbors with $k = 32$.

Therefore, the objective function of the post-processing refinement optimization is

$$\mathcal{L} = \mathcal{L}_I(\mathcal{G}) + \mathcal{L}_I(\mathcal{T}(\mathcal{G})) + \lambda_c \mathcal{L}_{col} \quad (17)$$

We use $\lambda_c = 0.02$ in all the experiments presented in this paper.

B. Additional Results on Two-Part Dataset

We compare with related methods including PARIS [24], ArticulatedGS [11], DTA [45], ArtGS [33] on the two-part object dataset. Since we take RGBD images as input, we apply the depth loss to PARIS [24] and ArticulatedGS [11] methods for a fair comparison. We report the quantitative evaluation results in Table 4, showing that the 3DGS-based methods, i.e. ArticulatedGS [11], ArtGS [33], and ours, achieve competitive performance. This is because static and movable parts can be well initialized with spatial clustering for two-part objects, which are further refined with

Table 4. Results on the PARIS [24] dataset, including both synthetic and real data. Methods marked with an asterisk (*) denote versions with added depth supervision for fair comparison. Specifically, ArticulatedGS* and PARIS* are trained with an additional depth loss.

		Synthetic Objects											Real Objects			
		FoldChair	Fridge	Laptop	Oven	Scissor	Stapler	USB	Washer	Blade	Storage	All	Fridge	Storage	All	
Axis	PARIS* [45]	15.79	2.93	0.03	7.43	16.62	8.17	0.71	0.71	41.28	0.03	9.37	1.90	30.10	16.00	
	ArticulatedGS [11]	6.20	0.14	15.55	0.00	<i>0.07</i>	0.08	0.16	0.03	0.23	0.04	2.25	4.06	48.56	26.31	
	ArticulatedGS*	<i>0.02</i>	0.12	0.03	0.13	0.18	0.13	0.12	0.17	<i>0.04</i>	0.04	0.10	64.81	29.44	47.12	
	Ang	DTA [45]	0.03	<i>0.09</i>	0.07	0.22	0.10	0.07	<i>0.11</i>	0.36	0.20	0.09	0.13	2.08	13.64	7.86
	ArtGS [33]	0.01	0.03	<i>0.01</i>	<i>0.01</i>	0.05	0.01	0.04	<i>0.02</i>	0.03	0.01	0.02	2.09	3.47	2.78	
	Ours	0.04	0.03	0.00	<i>0.01</i>	0.05	<i>0.04</i>	0.04	0.01	0.07	<i>0.02</i>	<i>0.03</i>	1.92	1.02	1.47	
Pos	PARIS* [45]	0.25	1.13	0.00	0.05	1.59	4.67	3.35	3.28	-	-	1.79	0.50	-	0.50	
	ArticulatedGS [11]	4.93	0.00	0.16	0.03	0.00	0.02	0.63	0.00	-	-	0.72	1.71	-	1.71	
	ArticulatedGS*	0.00	0.02	0.00	0.02	0.00	0.02	<i>0.64</i>	<i>0.02</i>	-	-	0.09	2.71	-	2.71	
	DTA [45]	<i>0.01</i>	<i>0.01</i>	<i>0.01</i>	<i>0.01</i>	<i>0.02</i>	0.02	0.00	0.05	-	-	<i>0.02</i>	0.59	-	0.59	
	ArtGS [33]	0.00	0.00	<i>0.01</i>	0.00	0.00	<i>0.01</i>	0.00	0.00	-	-	0.00	<i>0.47</i>	-	<i>0.47</i>	
	Ours	0.00	0.00	0.00	0.00	0.00	0.00	0.00	0.00	-	-	0.00	0.34	-	0.34	
Part Motion	PARIS* [45]	127.34	45.26	0.03	9.13	68.36	107.76	96.93	49.77	0.36	<i>0.30</i>	50.52	1.58	0.57	1.08	
	ArticulatedGS [11]	59.08	0.55	28.16	0.13	<i>0.05</i>	0.07	0.27	0.00	<i>0.04</i>	0.00	8.84	15.11	0.53	7.82	
	ArticulatedGS*	0.26	0.12	0.07	0.31	0.13	0.09	0.10	0.09	0.00	0.00	0.12	39.58	0.32	19.95	
	DTA [45]	0.10	0.12	0.11	0.12	0.37	0.08	0.15	0.28	0.00	0.00	0.13	1.85	<i>0.14</i>	1.00	
	ArtGS [33]	0.03	<i>0.04</i>	<i>0.02</i>	0.02	0.04	0.01	0.03	<i>0.03</i>	0.00	0.00	0.02	1.94	0.04	0.99	
	Ours	<i>0.06</i>	0.03	0.00	<i>0.03</i>	0.04	<i>0.05</i>	<i>0.04</i>	0.04	0.00	0.00	<i>0.03</i>	2.76	0.04	1.40	
CD-s	PARIS* [45]	10.20	8.82	<i>0.16</i>	3.18	15.58	2.48	1.95	12.19	1.40	8.67	6.46	11.64	20.25	15.95	
	ArticulatedGS [11]	3.17	2.02	4.27	2.31	<i>0.37</i>	1.84	1.88	5.17	0.44	2.74	2.42	36.05	75.82	55.94	
	ArticulatedGS*	0.58	1.09	1.72	1.88	0.64	<i>1.45</i>	<i>1.24</i>	3.58	<i>0.24</i>	<i>1.93</i>	<i>1.44</i>	230.04	46.78	138.41	
	DTA [45]	0.18	0.62	0.30	4.60	3.55	2.91	2.32	4.56	0.55	4.90	2.45	2.36	10.98	6.67	
	ArtGS [33]	<i>0.26</i>	<i>0.52</i>	0.63	3.88	0.61	3.83	2.25	6.43	0.54	7.31	2.63	1.64	2.93	2.29	
	Ours	0.48	0.31	0.12	1.41	0.19	0.67	0.96	2.69	0.21	1.81	0.89	1.96	2.54	2.25	
CD-m	PARIS* [45]	17.97	7.23	0.15	6.54	16.65	30.46	10.17	265.27	117.99	52.34	52.48	77.85	474.57	276.21	
	ArticulatedGS [11]	36.61	2.29	24.90	0.96	<i>0.35</i>	1.64	<i>1.02</i>	3.88	1.86	5.49	7.90	107.96	2,459.45	1,283.71	
	ArticulatedGS*	0.33	0.63	2.07	1.08	0.57	1.97	1.17	<i>0.41</i>	0.78	0.83	<i>0.98</i>	69.23	1,578.02	823.63	
	DTA [45]	<i>0.15</i>	<i>0.27</i>	<i>0.13</i>	<i>0.44</i>	10.11	1.13	1.47	0.45	2.05	<i>0.36</i>	1.66	<i>1.12</i>	30.78	15.95	
	ArtGS [33]	0.54	0.21	<i>0.13</i>	0.89	0.64	0.52	1.22	0.45	<i>1.12</i>	1.02	0.67	0.66	6.28	3.47	
	Ours	0.11	0.28	0.07	0.33	0.18	<i>0.83</i>	0.37	0.08	F	0.35	0.28 ^F	28.31	35.95	32.13	
CD-w	PARIS* [45]	4.37	5.53	<i>0.26</i>	3.18	3.90	5.27	1.78	10.11	0.58	7.80	4.28	8.99	32.10	20.55	
	ArticulatedGS [11]	1.06	2.12	8.52	2.13	<i>0.35</i>	1.61	1.88	4.79	0.23	2.62	2.53	77.53	995.99	536.76	
	ArticulatedGS*	0.43	0.96	0.80	<i>1.60</i>	0.59	<i>1.48</i>	<i>1.00</i>	<i>3.08</i>	<i>0.20</i>	<i>1.75</i>	<i>1.19</i>	51.22	965.80	508.51	
	DTA [45]	<i>0.27</i>	0.70	0.32	4.24	0.41	1.92	1.17	4.48	0.36	3.99	1.79	2.08	8.98	5.53	
	ArtGS [33]	0.43	<i>0.58</i>	0.50	3.58	0.67	2.63	1.28	5.99	0.61	5.21	2.15	<i>1.29</i>	<i>3.23</i>	<i>2.26</i>	
	Ours	0.10	0.31	0.09	1.32	0.18	0.62	0.50	2.40	0.18	1.60	0.73	1.03	2.03	1.53	

the following deformable 3DGS optimization. This experiment also acts as a sanity check for our method, validating that the over-segmentation proposals from the same movable part can be effectively merged based on their motion similarities.

Figure 8 provides the full visualization results of ArtGS and Ours on this dataset. The results demonstrate that our method can robustly integrate the proposals and reconstruct both the part probability field and motion parameters. For incorrectly initialized mobility proposals, our optimization can also obtain correct motion estimation and the final reconstructions. For the real-world objects in this dataset, our method’s performance on the geometry reconstruction, especially in terms of CD metric, is limited by the quality of input depth maps. This is because our method tends to estimate the mobility parameters that align the transformed

results closer to the depth map of state $t = 1$. Large discrepancies between the input depth maps of states $t = 0$ and $t = 1$ lead to our results containing a small number of Gaussians originating from static part, such as the Real Storage in Figure 8 and Figure 13.

C. Additional Results on Multi-Part Dataset

We present a comprehensive visual analysis to compare ArtGS [33] and our method in Figure 9 and Figure 11, which show the reconstructed articulated objects at different motion states and their articulated joints of movable parts. Compared to ArtGS, our method can robustly estimate the movable parts and motion parameters, leading to consistent and clean rendered images of the reconstructed objects.

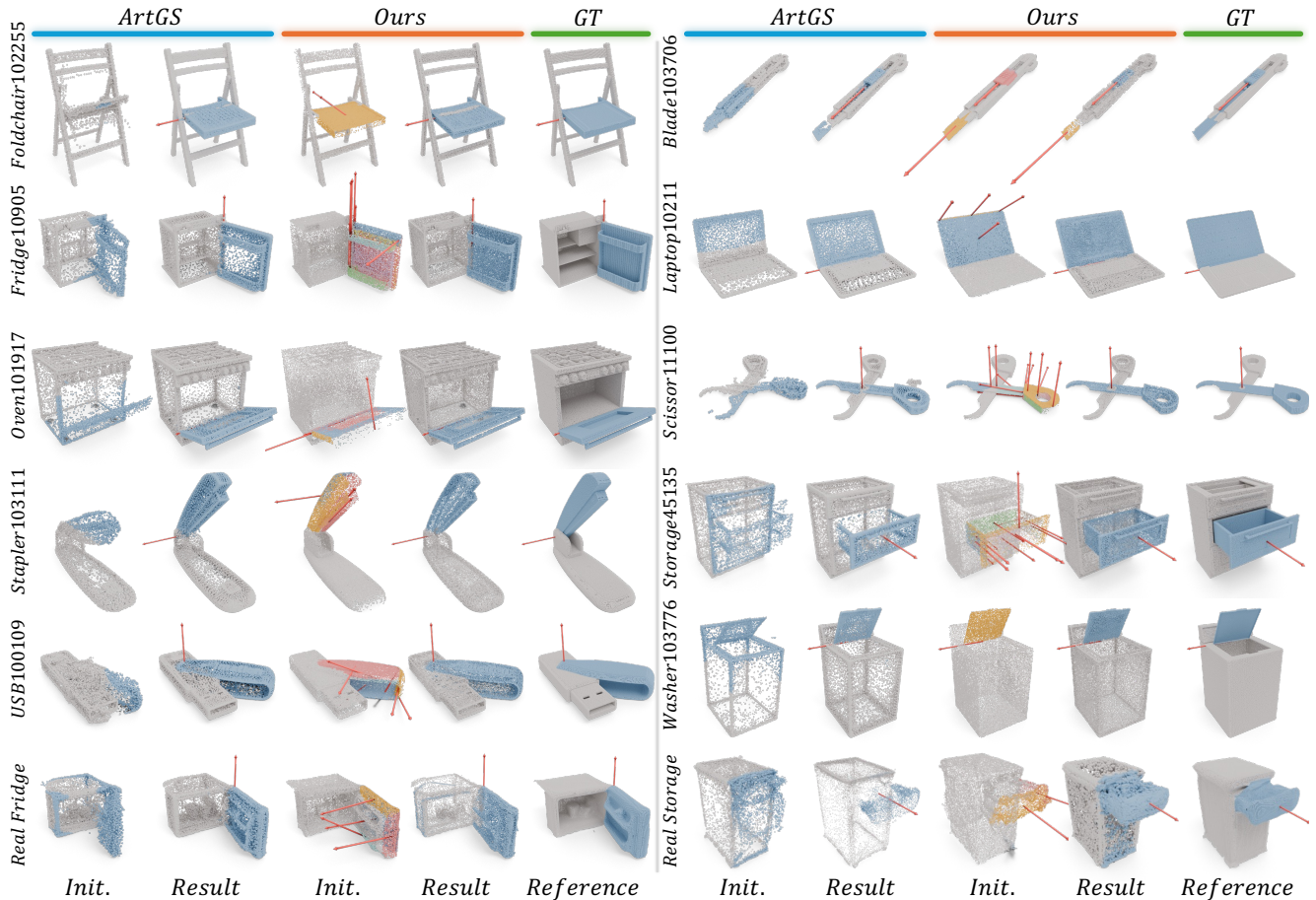


Figure 8. Additional qualitative results on PARIS dataset, including the initializations and the final reconstructions. We show the Gaussians with their center points for a better visualization of their segmentation and motion parameters.

D. More Visual Analysis on Multi-Part Dataset

We further show the visualizations of the initializations and reconstructed results of ArtGS and ours in Figure 10 and Figure 12. The results show that our mobility initialization can effectively extract the potential movable parts and reasonable motion initialization, while ArtGS suffers from unstable initialization. For over-segmented proposals, our optimization can effectively estimate their motion parameters and integrate adjacent proposals into an individual part.

E. Failure Cases

Although our approach achieves much more robust motion estimation and reconstruction of articulated objects than existing approaches, it still suffers from the common issues of the self-supervised 3DGS reconstruction framework. We show two representative failure cases in Figure 13. First, since our method lacks semantic part segmentation supervision for separating the adjacent movable parts, it sometimes causes the part boundary to encroach on neighboring part

regions, such as the interior and the edge of the drawers in Figure 13. Second, the estimation of mobility parameters in our method primarily relies on the depth component of the RGBD loss \mathcal{L}_I and the geometry-aware Chamfer distance loss \mathcal{L}_{cd} . Consequently, the accuracy of these estimations is highly dependent on the input depth map quality. In scenarios where the acquired depth maps contain significant inaccuracies, due to factors such as sensor noise, occlusions, or varying illumination conditions, the optimization process can be misled. As illustrated in Figure 13 (using real-world data from the PARIS dataset), this can cause our method to erroneously incorporate Gaussians from the static part into the estimated movable part. To achieve a lower loss value under these incorrect constraints, the optimization incorrectly transforms the movable part into the interior of the object. It is worth noting that in our real-world reconstruction experiments, the quality of the mobility results has been significantly improved by enhancing the input depth maps using the pre-trained Depth-Anything-V2 model [52] which effectively mitigates these issues.

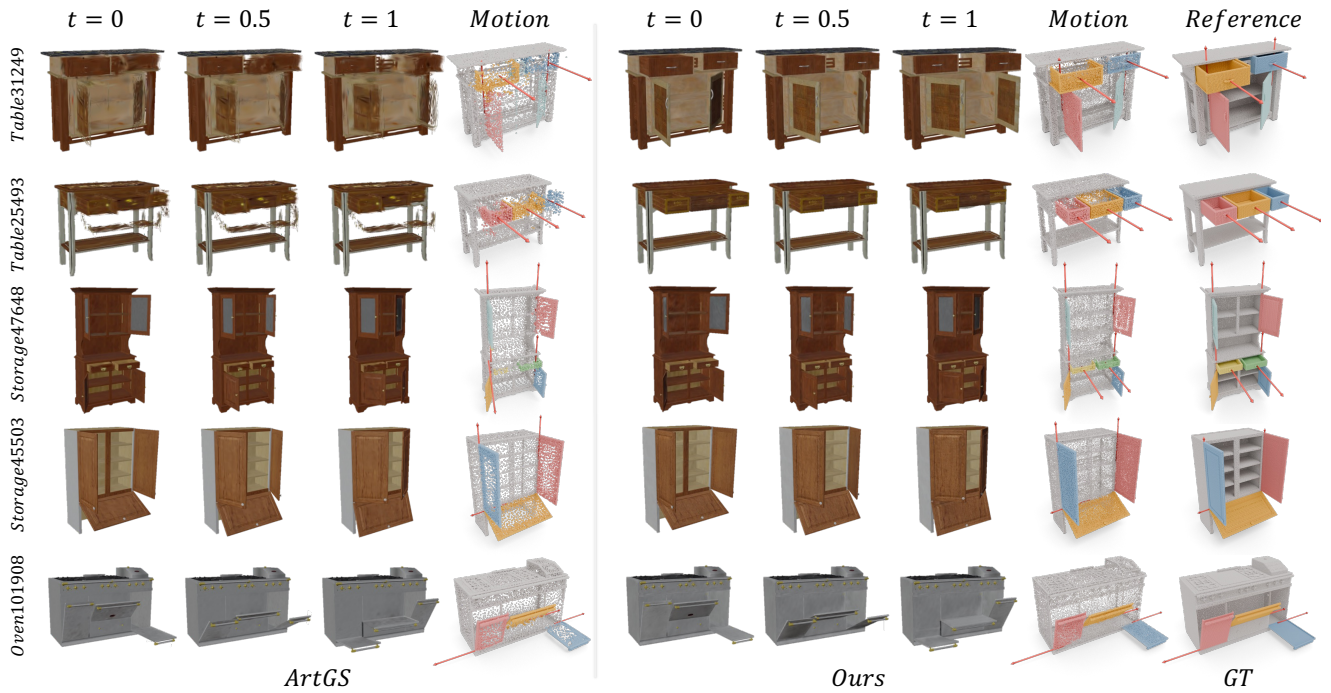


Figure 9. Additional reconstruction results on **ArtGS-Multi dataset**. We render the reconstructed articulated objects in different motion states ($t \in \{0, 0.5, 1\}$) and their motion structures for each result.

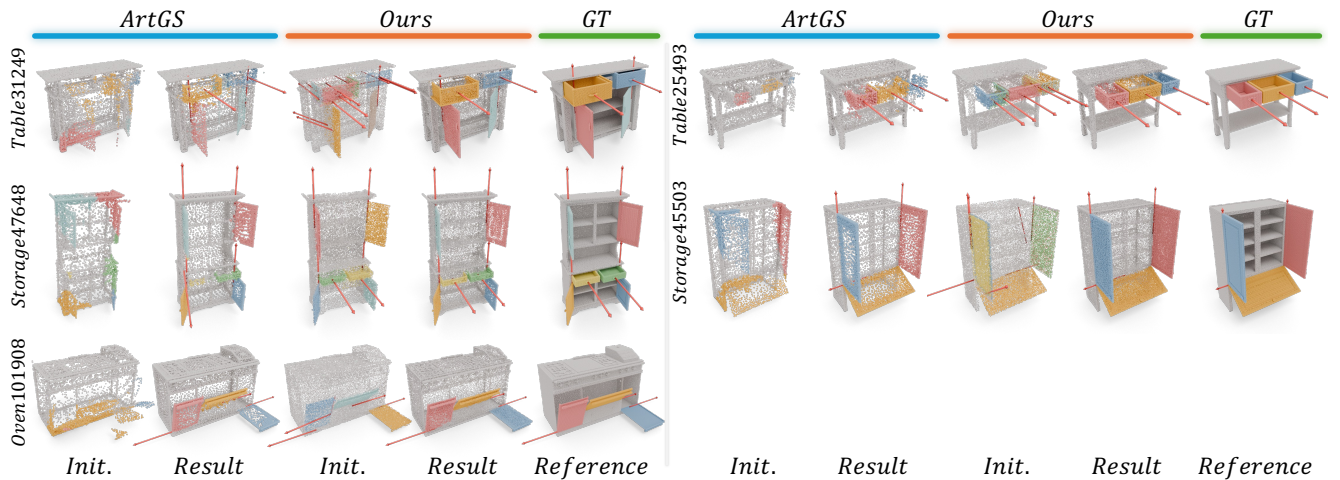


Figure 10. Additional qualitative results on **ArtGS-Multi dataset**, including the initializations and the final reconstructions. We show the Gaussians with their center points for a better visualization of their segmentation and motion parameters.

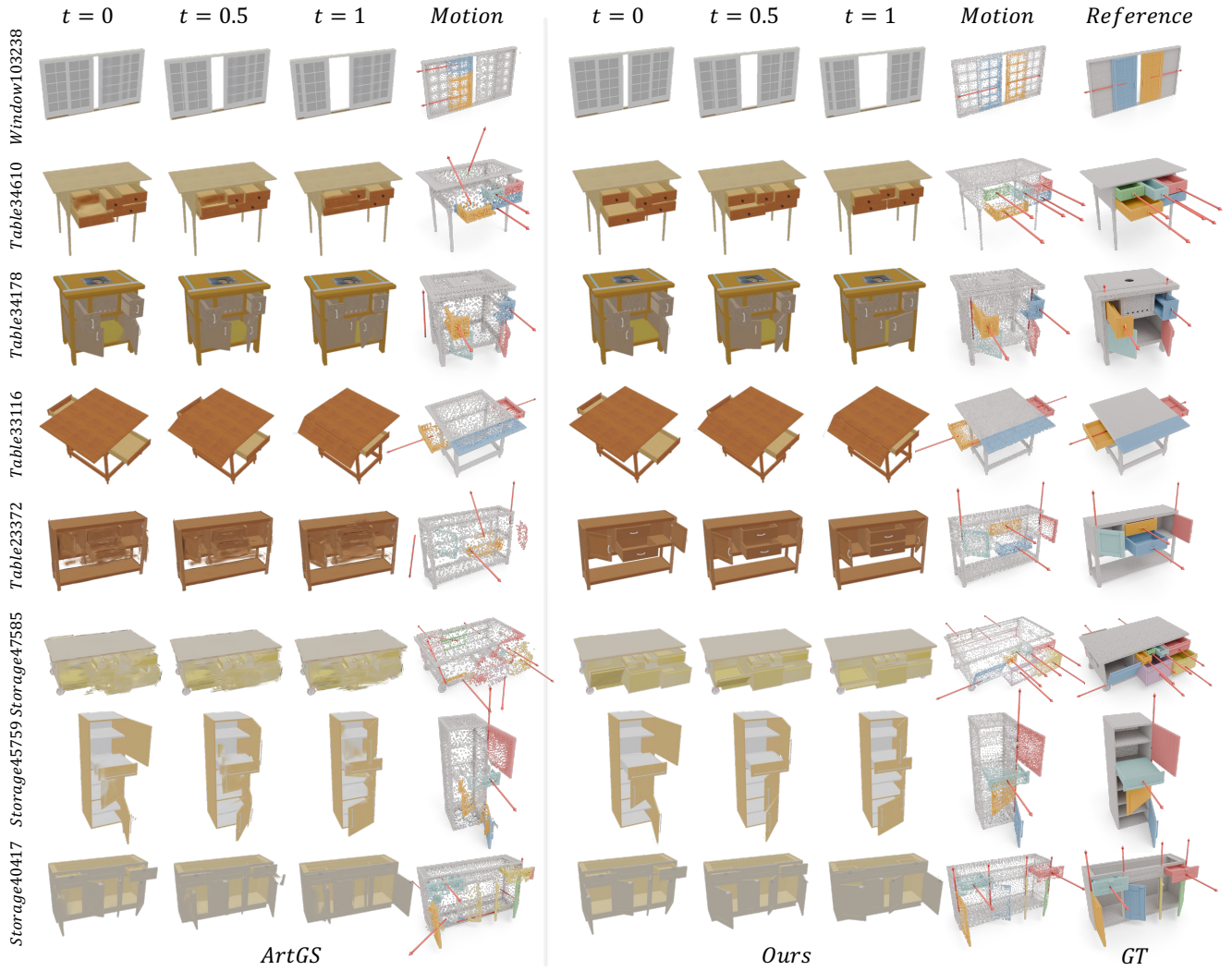


Figure 11. Additional reconstruction results on **our dataset**. We render the reconstructed articulated objects in different motion states ($t \in \{0, 0.5, 1\}$) and their motion structures for each result.

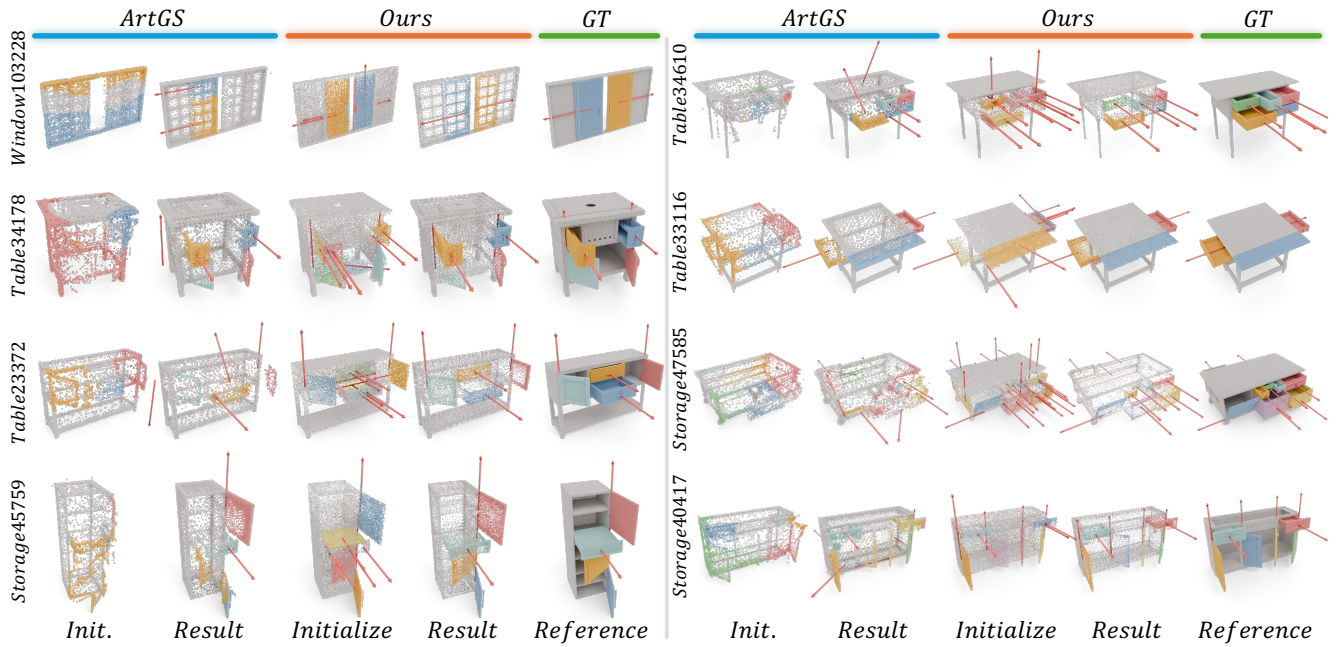


Figure 12. Additional qualitative results on **our dataset**, including the initializations and the final reconstructions. We show the Gaussians with their center points for a better visualization of their segmentation and motion parameters.

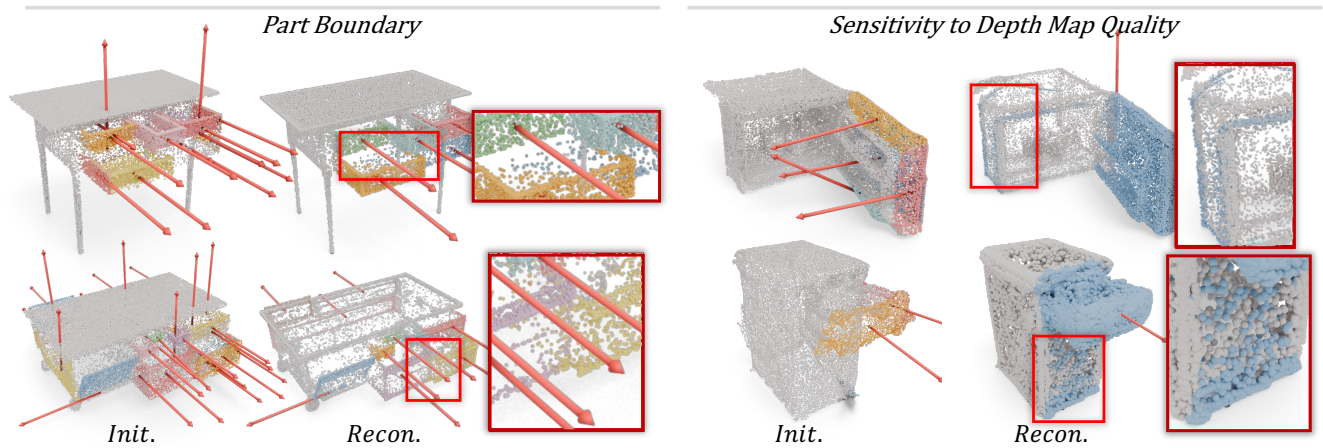


Figure 13. Failure cases. We illustrate failure cases of low-quality part boundaries. For low-quality RGBD images input, our method difficult to reconstruct the part boundaries.